Thermochimica Acta 693 (2020) 178779

Contents lists available at ScienceDirect

Thermochimica Acta

journal homepage: www.elsevier.com/locate/tca

In situ calibration of an uncooled thermal camera for the accurate quantification of flower and stem surface temperatures

Ryan A.E. Byerlay [a,*], Charlotte Coates [a], Amir A. Aliabadi [b], Peter G. Kevan [a]

[a] School of Environmental Sciences, University of Guelph, Guelph, Ontario, Canada
[b] School of Engineering, University of Guelph, Guelph, Ontario, Canada

ARTICLE INFO

Keywords:
Thermal imaging
Radiometric calibration
Thermography
Plant temperature

ABSTRACT

This paper presents an in situ calibration method for an uncooled thermal camera to reduce bias and root mean square error (RMSE) for the observed surface temperatures of *Gerbera jamesonii* plants. Surface temperature bias and RMSE were quantified for the calibrated camera constants and compared with respect to the default constant statistics. The averaged calibrated camera constant bias and RMSE values decreased by at least 89.1% relative to the averaged default camera constant bias and RMSE values for individual plant stems and flowers. This calibration approach has the potential to be suitable for other uncooled thermal cameras in fields beyond horticultural applications.

1. Introduction

Vegetative surface temperature (ST) is an important biophysical variable which is known to impact environmental and biological processes [1,2]. Accurate and precise quantification of vegetative ST is an important consideration for precision agriculture applications and for environmental phenomena, especially for understanding impacts of micro-climates in urban, rural, agricultural, alpine, and arctic regions, Earth energy balance models, and more broadly, climate change models [3–8]. Remote sensing systems including satellites and unmanned aerial systems (UASs) (such as drones), equipped with thermal imaging systems have historically been used to quantify vegetative ST and other important crop variables including soil moisture and evapotranspiration [9,10]. ST data derived from remote sensing systems is highly influenced by atmospheric effects, limited spatial resolution (for satellite-based sensors), and radiometric accuracy, especially for uncooled thermal cameras [10–12]. As a result, conventional thermal remote sensing methods are not suitable to accurately quantify ST of individual plants.

Radiometric thermal imaging cameras have been noted in literature to record STs of plants and plant organs (see Table 1 for details). It is important to note that each study used an uncooled long-wavelength infrared (LWIR) radiometric thermal camera to quantify ST except for the Lamprecht et al. [13] study, which used a cooled mid-wavelength infrared (MWIR) camera. Both MWIR (3–5 μm band) and LWIR (8-15 μm band) cameras have been used to quantify ST in literature [14, 15]. MWIR sensors on satellites have been used to identify high temperature targets such as wildfires, and LWIR sensors have been used to quantify Earth surface temperatures [16]. MWIR cameras are known to be preferred over LWIR cameras in marine environments and areas with high relative humidity [15]. Most MWIR camera detectors are cooled while LWIR camera detectors can either be cooled or uncooled [17,18]. Cooled thermal cameras provide more accurate and precise ST data as compared to uncooled thermal cameras [18,19]. However, cooled thermal cameras are significantly more expensive, physically larger, heavier, and require more power to operate as compared to uncooled thermal cameras [17–19]. As a result, uncooled cameras can be used on UASs but are less accurate as the LWIR detector can be influenced by camera and ambient temperatures [12,20]. Uncooled thermal cameras are calibrated in a laboratory by the manufacturer of the device. However, the radiometric accuracy of images recorded during fieldwork can be highly variable as camera and ambient temperatures directly impact the observed thermal radiation [20–23]. Through the completion of an in situ calibration of STs for different materials, it is possible to reduce uncooled thermal camera errors and to achieve higher accuracies compared to manufacturer specifications [23–25]. A procedure to acquire very accurate ST for individual plant organs is desired for concurrent research related to understanding thermal regimes within hollow stem plants [26].

1.1. Objectives

In this paper, an in situ method to radiometrically calibrate an

* Corresponding author.

https://doi.org/10.1016/j.tca.2020.178779
Received 3 July 2020; Received in revised form 8 September 2020; Accepted 10 September 2020
Available online 17 September 2020

Table 1
Previous horticultural studies employing thermal cameras for radiometric quantification of STs in reverse chronological order.

Reference	Year published	Camera model	Camera calibration performed	Application
[27]	2019	FLIR Tau 2	Yes, specifics of calibration are not detailed	Measured canopy temperature variations of apple trees
[1]	2017	FLIR E60bx	No	Measured floral temperature patterns with respect to other plant organs
[28]	2016	FLIR T440	No	Measured leaf temperature to identify plant stress in *Ascophyllum nodosum*
[29]	2013	VarioCAM (384 by 288 pixels)	No	Measured maize canopy temperatures to identify genotypes tolerant to water-stress
[30]	2013	FLIR i5	No	Measured leaf temperature of *Sorghum bicolor* (L.) Moench
[31]	2013	Miricle 307 K	Yes, in laboratory	Measured canopy temperature of grapevines
[32]	2012	FLIR B360	No	Measured canopy temperatures to quantify plant water status indicators
[13]	2006	Inframetrics SC1000	No	Measured ST of blossoms

uncooled thermal camera with respect to five varieties of *Gerbera jamesonii* (*Gerbera* daisy) flowers and stems at a commercial greenhouse located in Grimsby, Ontario, Canada is detailed. Variables inherent to the thermal camera were calibrated and relevant statistics were computed and compared with respect to manufacturer calibrated values. Images were collected at varying times over four different days during January–February 2020.

This paper is structured as follows: the instruments used and methods followed during the experiment and the detailed mathematical theory behind thermal imaging principles are included in Section 2. Section 3 contains the results and statistics from the in situ calibration and a discussion of the results is included. Lastly, Section 4 concludes the paper and highlights future work goals.

2. Materials and methods

2.1. Experimental materials

The thermal images were collected using a FLIR E6 handheld uncooled thermal camera. STs of the flowers and stems were quantified using a calibrated Omega Type K thermocouple equipped to an Omega OM-HL-EH-TC data logger. The experiments were conducted at Van Geest Bros. Limited in Grimsby, Ontario, Canada inside a commercial greenhouse facility (see Fig. 1 for the *Gerbera* daisy arrangement). A diagram of the experimental setup is depicted in Fig. 2.

Gerbera is a genus of plants in the sunflower family, *Asteraceae*. The morphology of the *Gerbera* daisy varieties differ in floral color and size, and in stem thickness and structure. The stem characteristics may be hollow, solid, or spongey. Plants within same variety have similar color, size, and stem types. The five *Gerbera* daisy varieties included in

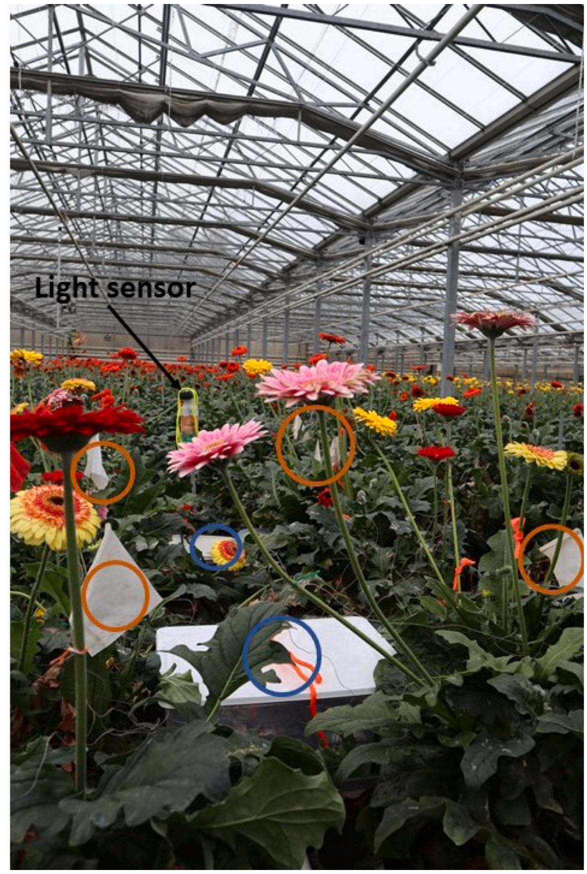

Fig. 1. The greenhouse and *Gerbera* daisy arrangement at the commercial facility, where the orange circles highlight white flags which represent some of the plants imaged in this paper, the blue circles indicate thermocouple-data logger systems which monitored internal stem and ambient stem temperatures, and the light sensor recorded light intensity. Concurrently with the thermal imaging study, internal and external temperature and light intensity data was collected for an ongoing research project. (For interpretation of the references to color in this figure legend, the reader is referred to the web version of this article.)

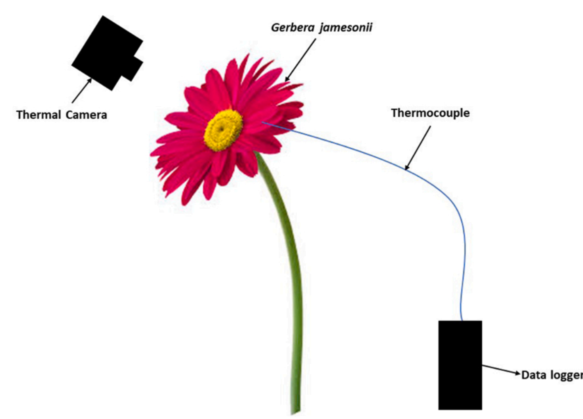

Fig. 2. Diagram of the experimental setup in the greenhouse.

this experiment are all large daisies which include Prestige, Brunello, Panama, Rendez-Vous, and Toast (see Fig. 3). In total, six different *Gerbera* daisies, including two *Gerbera* daisies of the Prestige variety, were imaged in this experiment. It is important to note that the Toast variety is known to have a variable stem structure. Concurrently, ambient temperatures around *Gerbera* daisy stems and internal hollow

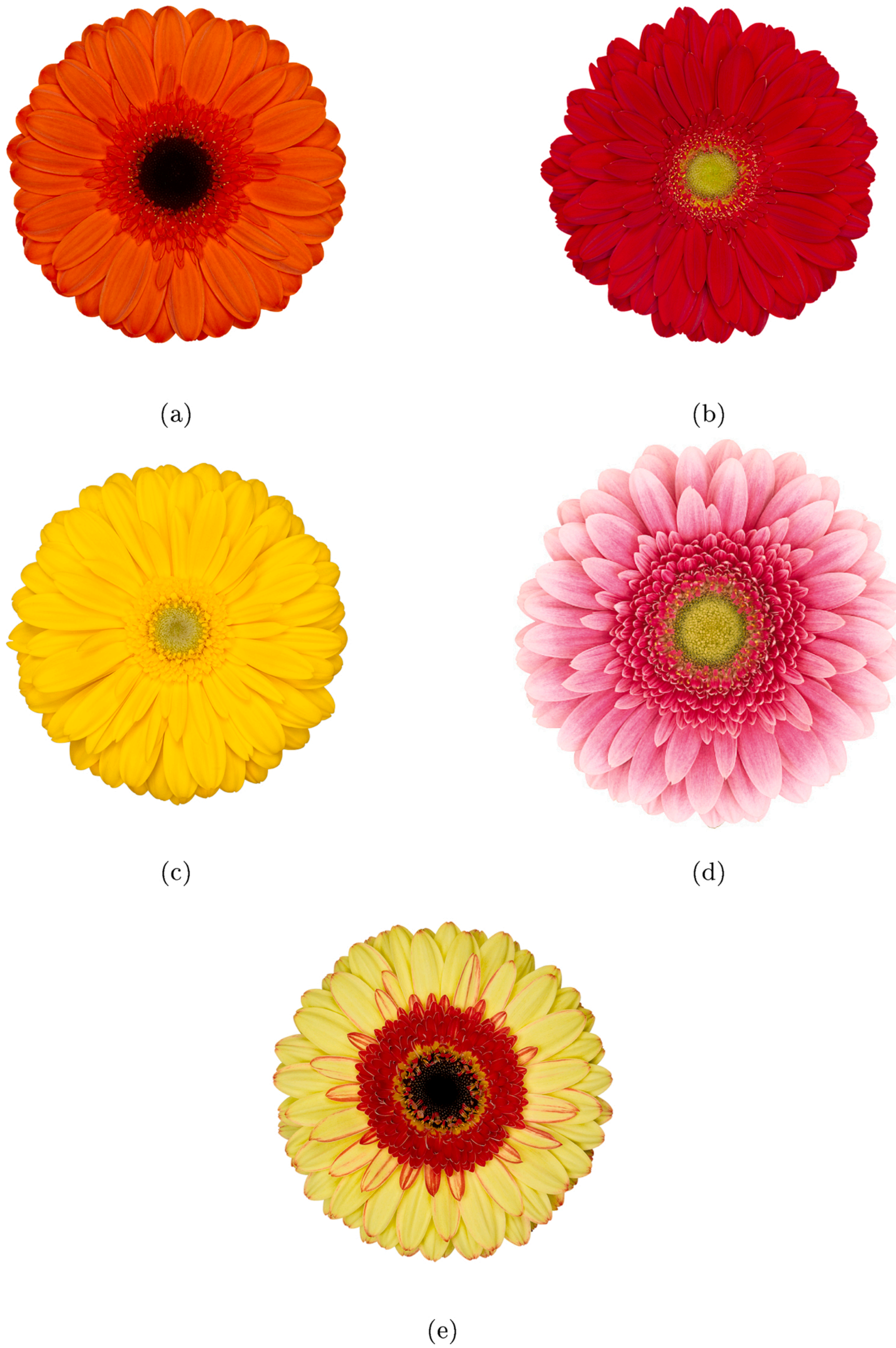

Fig. 3. The *Gerbera* daisy varieties recorded by the thermal camera including: (a) Prestige, (b) Brunello, (c) Panama, (d) Rendez-Vous, and (e) Toast. Source: Van Geest Bros. Limited.

stem temperatures of each variety were also being recorded by Omega Type K thermocouples and Omega OM-HL-EH-TC data loggers. Ongoing research is being conducted to investigate the micro-meteorological phenomena of temperature regimes in hollow stem plants [26].

The FLIR E6 thermal camera has an uncooled microbolometer detector which is sensitive to LWIR radiation within the 7.5-13 μm band. The system also contains a digital camera which records pictures within the visible light spectrum with a resolution of 640 by 480 (horizontal by vertical pixels). The infrared resolution of the camera is 160 by 120. The camera has a radiometric precision of less than 0.06 K and an accuracy of ±2 K or 2% of the reading if the ambient temperature is between 283 and 308 K and the object temperature is above 273 K. The horizontal and vertical fields of view are 45° and 34° respectively. The camera has a pixel pitch of 17 μm and an instantaneous field of view of 5.2 mrad. The Omega OM-HL-EH-TC data logger was equipped with one Omega Type K thermocouple that measured temperature every minute. The accuracy of the thermocouple-data logger system is 0.8 ± 2% K and has a resolution of 0.1 K. The data logger is capable of recording temperatures between 73 and 2073 K.

2.2. Experimental method

Thermal images and STs of individual plants were recorded on January 24, 2020 between 11:29 and 12:04 Eastern Standard Time (EST = GMT − 5), January 30, 2020 between 14:01 and 14:23 EST, February 6, 2020 between 10:37 and 10:57 EST, and February 12, 2020 between 9:09 and 9:28 EST. The environmental conditions within the greenhouse were known to be diurnally variable and it is anticipated that future field work will occur between the hours of 09:00 and 15:00 EST. As a result, images were recorded over a range of times to account for the variable environmental conditions in the greenhouse which are known to directly impact uncooled radiometric imaging systems and result in inaccurate ST values [20,22,25,33]. For instance, water vapor is known to absorb infrared radiation [34,35]. As a result, environments with a high relative humidity may reduce thermal imaging accuracy. This phenomenon was documented by Mangus and Sharda [36] and was especially noticeable when considering increasing relative humidity for object STs greater than 5 K above ambient temperature (R^2 of 0.5212) or when object STs are greater than 5 K below ambient temperature (R^2 of 0.7073). When the object temperature is equivalent to ambient temperature, accuracy slightly decreases as relative humidity increases, however the R^2 value is 0.0439. Mangus and Sharda hypothesized this slight inaccuracy occurred due to variations in ambient air particle temperature between the imaged object and the thermal imaging system.

Prior to imaging, the camera was turned on for approximately 5 min (as recommended in the FLIR E6 manual) to acclimate to the greenhouse environment and to ensure as accurate as possible results. During each measurement, the thermocouple attached to the Omega data logger was placed on the surface of either the stem or ray floret of each plant. Concurrently, the thermal camera was positioned at an oblique angle, with respect to the plant organ plane, approximately 30 cm away from the imaged surface and thermocouple. It was ensured that the thermocouple was visible in the thermal camera's field of view before recording the image. It is known that oblique angle thermal images can significantly impact the fraction of observed reflected longwave radiation. This phenomenon is well documented when recording oblique angle images over waterbodies where observed surface emissivity can vary as a function of camera pitch angle [37–39]. Oblique angle thermal images recorded over terrestrial surfaces are also known to be impacted by the fraction of observed reflected longwave radiation [40–43]. The FLIR thermal camera used in this experiment did not contain an inertial measurement unit and as a result, the exact pitch and yaw angles for each image are unknown. However, according to FLIR-sUAS [44], oblique angle images recorded within 60° of nadir are optimal to minimize errors associated with the reflection of long wave radiation. It is estimated that all oblique angle thermal images were recorded between 10° and 50° of nadir.

On each day, three thermal images of each *Gerbera* daisy variety stem and ray floret were recorded. Approximately 30 s elapsed between individual measurements to account for thermal drift of the camera which can alter ST measurements by over 1 K per minute [23,45]. This process was repeated for the stem and flower of each plant. All thermocouple data was recorded in a notebook as observed from the data logger.

2.3. Surface temperature quantification

Uncooled thermal cameras create a signal response (referred to as A/D counts) for each pixel of an image when LWIR radiation is incident to the microbolometer. A/D counts are directly proportional to the amount of LWIR radiation passing through the camera lens onto the thermal detector. A non-linear relation can be used to convert A/D counts to temperature by considering four constants that are intrinsic to the uncooled thermal camera. This non-linear relation is derived from the Planck's Law and is represented in Eq. (1)

$$T_{\mathrm{Obj}} = \frac{B}{ln\left(\frac{R}{U_{\mathrm{Obj}}+O}+F\right)}, \tag{1}$$

where T_{Obj} represents the imaged object ST in Kelvin, U_{Obj} represents the pixel signal value recorded as A/D counts of the imaged object, and B, R, O, and F are all constants related to Planck's Law and represent Planck's radiation law, the response of the uncooled camera, an offset value, and a value for the alignment of the non-linear response of the camera system, respectively [20]. These four constants are calibrated by the manufacturer and are included in the metadata of each image. The constants are highly dependent on the specific camera and cannot be used interchangeably between camera models. Eq. (1) can be rearranged to quantify A/D counts as per Eq. (2)

$$U_{\mathrm{Obj}} = \frac{R}{exp\left(\frac{B}{T_{\mathrm{Obj}}}\right)-F} - O, \tag{2}$$

Thermal cameras are known to observe LWIR radiation from three separate sources including the imaged object, radiation reflected from the imaged object, and radiation transmitted from the atmosphere. The total radiation observed by a thermal camera can be represented with Eq. (3)

$$U_{\mathrm{Tot}} = \epsilon\tau U_{\mathrm{Obj}} + \tau(1-\epsilon)U_{\mathrm{Refl}} + (1-\tau)U_{\mathrm{Atm}}, \tag{3}$$

where U_{Tot} represents the total signal in A/D counts recorded by the uncooled thermal camera, U_{Refl} represents the fraction of reflected radiation from the imaged object in A/D counts, U_{Atm} represents the fraction of radiation transmitted from the atmosphere and observed by the thermal camera, ϵ represents the emissivity of the imaged object, a physical property of the material, and τ represents the atmospheric transmissivity, which is a function of the object distance from the camera and atmospheric conditions such as the relative humidity [46].

For this research, Eqs. (1) and (2) are of most importance. The four constants are intrinsic properties of the thermal camera which directly affect the ST measurement. From image metadata and FLIR Tools, the original four constants as calibrated by the manufacturer and the ST of flowers and stems were obtained. Using the four constants and Eq. (1), U_{Obj} values were quantified and were used during the radiometric calibration procedure.

The calibrated constants are evaluated with respect to the original camera manufacturer constants (default constants) considering bias and root mean square error (RMSE) represented by Eqs. (4) and (5) respectively:

$$\mathrm{Bias} = \frac{1}{n}\sum_{i=1}^{n}(C_i - R_i), \tag{4}$$

$$\mathrm{RMSE} = \sqrt{\frac{1}{n}\sum_{i=1}^{n}(C_i - R_i)^2}, \tag{5}$$

where n represents the total number of measurements, C_i represents the surface temperature measured by the thermal camera for each i$^{\mathrm{th}}$ measurement, and R_i represents the thermocouple temperature for each i$^{\mathrm{th}}$ measurement.

2.4. Thermal camera calibration

The Type K thermocouple attached to the Omega data logger was calibrated in Guelph, Ontario, Canada via a two-point calibration. Three measurements were recorded when the thermocouple was submerged in an ice water bath and another three measurements were recorded when submerged in boiling water. Thirty seconds elapsed between each respective measurement. The mean of the three measurements were used during the radiometric calibration procedure. All thermocouple temperatures collected in Grimsby, Ontario, Canada were corrected prior to quantifying the calibrated thermal camera constants. The corrected thermocouple data for each plant organ was averaged for each day prior to completing the radiometric calibration procedure.

Using FLIR Tools, the location of the thermocouple in relation to the flower and stem of each *Gerbera* daisy was identified. A box (four pixels wide by four pixels high) was manually drawn around the thermocouple placed on each flower and stem. The resulting average temperature of the box was extracted from FLIR Tools to represent the ST measured by the camera. See Fig. 4 for an example of a thermal image and the digital image recorded by the thermal camera system. Using ExifTool 10.86, the uncooled thermal camera constants as calibrated by the manufacturer were identified. The four constants were used in Eq. (2) to calculate the U_{Obj} values. The U_{Obj} values for each plant organ were averaged for each day prior to camera calibration. It should be noted that the location of the thermocouple could not be identified in a few images recorded during the experiment as they were obscured by the researcher's hand when positioning the thermocouple. These images were omitted from the analysis.

The averaged thermocouple temperature data and the averaged U_{Obj} values from the thermal camera were imported into a Python 3.6 script. The empirical line method, as discussed by Smith and Milton [47], was used to plot U_{Obj} values with respect to the corresponding thermocouple temperature values. These plots are illustrated in Figs. 5 and 6 . the non-linear least-squares minimization and curve-fitting (LMFIT) library Version 1.0.0 from Python was used with Eq. (1) to fit the data and optimize the camera constants for the flowers and stems of each *Gerbera* daisy variety. The default camera constants from the manufacturer were used as the initial guesses (see Table 2), the minimum values (50% of the manufacturer (default) constants), and the maximum values (150% of the manufacturer (default) constants) of each default camera constant were used as bounds with the LMFIT library to optimize the calibrated camera constants and minimize residuals. The bias and RMSE statistics of the ST for the calibrated constants and for the default constants are tabulated in Table 3 for plant stems and in Table 4 for flowers. The averaged values for the default and calibrated bias and RMSE statistics are also reported for both stems and flowers.

Since two different Prestige plants were imaged, camera constants were derived for both the stem and the flower by combining temperature data of the two plants. The use of LMFIT and the method using the default constants as the initial guesses, and bounding the minimum and maximum values, were repeated for each case. Fig. 7 displays the calibration for the stem and the flower of the combined Prestige plants. Bias and RMSE statistics of the ST were calculated accordingly and are represented in Table 5. Lastly, the calibrated camera constants of one specific Prestige plant were used with the thermocouple ST and U_{Obj} values of the other Prestige plant. ST statistics for this case are depicted in Table 6.

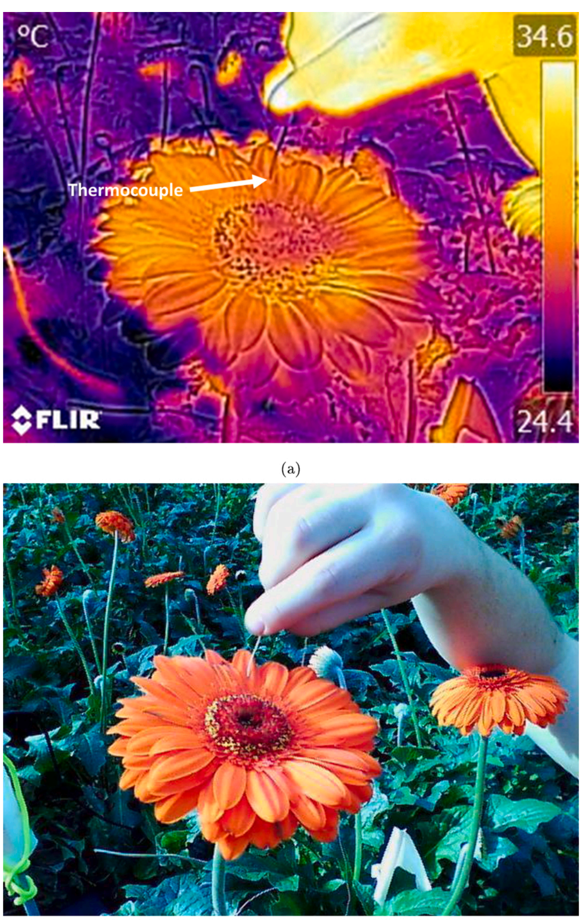

(a)

(b)

Fig. 4. (a) Thermal image analysis of a Prestige flower recorded on January 24, 2020, where temperature is displayed as degrees Celsius and the white arrow indicates the tip of the thermocouple; (b) corresponding digital image of the Prestige flower recorded by digital camera of the FLIR E6.

3. Results and discussion

The calibrated bias and RMSE decreased and improved relative to the uncalibrated statistics for the plant stems and flowers. Considering the calibrated statistics for each individual plant in Tables 3 and 4, the calibrated bias and RMSE were all reduced relative to the default statistics. The calibrated RMSE decreased by at least one order of magnitude for all cases. It is also important to note that the STs quantified with the default camera constants are consistently higher than the temperatures recorded in the calibration experiment and subsequently the STs quantified with the calibrated camera constants. As the imaged object temperature increases (A/D counts increase), this pattern becomes more pronounced and is prevalent in Figs. 5–7 .

The default and calibrated bias and RMSE values were averaged considering each *Gerbera* variety and were reported in the appropriate table. Specifically, averaged bias and RMSE values were calculated for the plant stems, flowers, and for the case considering calibrated camera constants for one Prestige plant and temperature data for the other Prestige plant. The averaged calibrated bias and RMSE values improved relative to the averaged default bias and RMSE values for both the plant stems (89.1% reduction for bias and 90.7% reduction for RMSE) and flowers (100.6% reduction for bias and 96.2% reduction for RMSE). For the third case considering the Prestige camera constants for one plant and temperature data for the other Prestige plant, the statistics were averaged with respect to the plant organ being imaged. Subsequently, the averaged calibrated biases for the stem and flower improved relative to the averaged default biases where the calibrated stem bias reduced by 68.4% and the calibrated flower bias reduced by 104.3%. Likewise, the averaged calibrated RMSE for the flower decreased relative to the averaged default RMSE by 56.8%. The averaged calibrated RMSE for the stem however increased relative to the averaged default RMSE by 90.2%. Since the temperature sample size is low and RMSE is known to be sensitive to outliers [48], it is possible for the calibrated RMSE to be skewed. It may be possible to reduce the averaged calibrated RMSE below the averaged default RMSE if more samples were recorded and outliers significantly larger than the data set were omitted from the RMSE calculation. Nonetheless, it is important to note that both the bias and RMSE generally decreased when considering the temperature statistics calculated from the calibrated camera constants.

For each *Gerbera* daisy, only four measurements were collected, however, two plants of the same variety (Prestige) were included in the experiment. The ST data from the two plants were combined and camera constants were calibrated. The resulting calibrated bias statistics

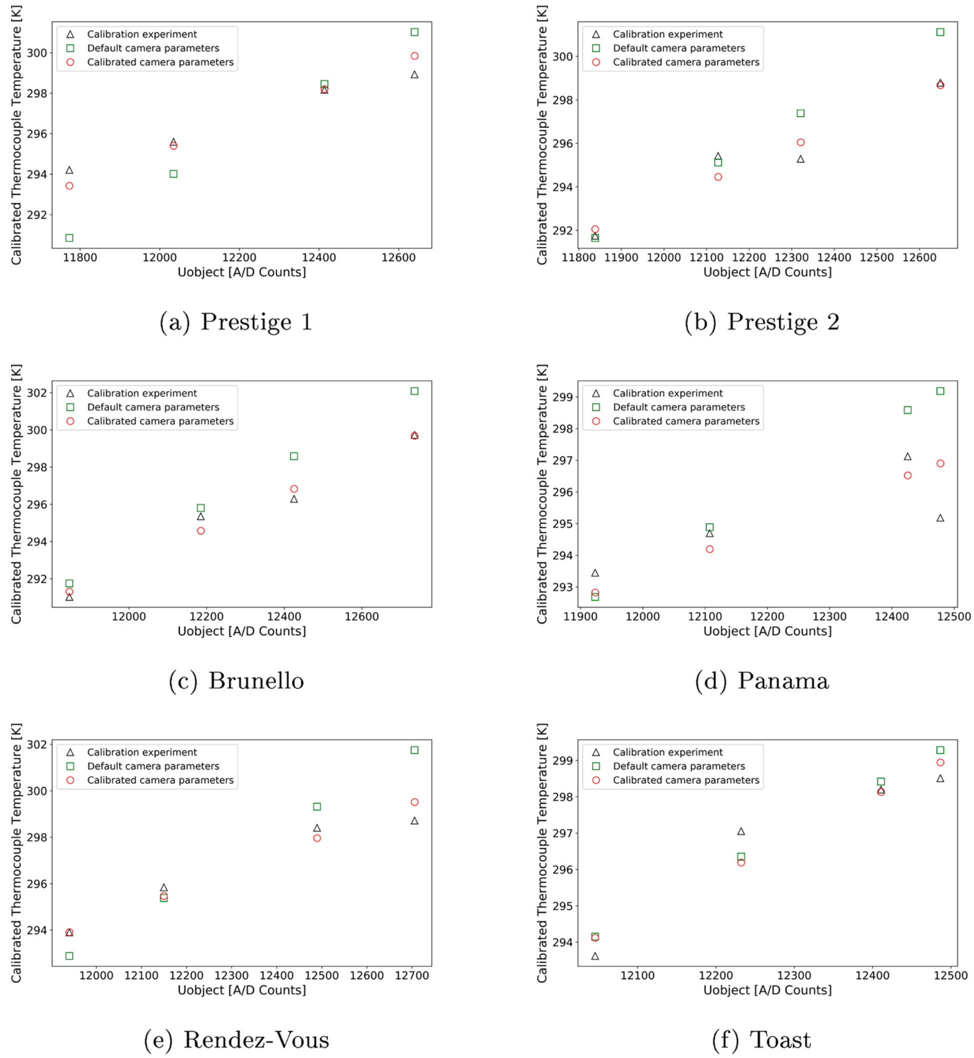

Fig. 5. Thermocouple temperature compared to radiometric image A/D counts values for the calibration experiment (black triangles), the default camera constants (green squares), and the calibrated camera constants (red circles) for each *Gerbera* daisy stem. The calibrated camera constants were used to quantify the calibrated temperatures. (For interpretation of the references to color in this figure legend, the reader is referred to the web version of this article.)

improved over the default values by reducing bias by 133% for stems and by 103% for flowers. Likewise, the resulting RMSE statistics improved over the default values by reducing RMSE by 66.7% for stems and by 96.5% for flowers. Ideally, more measurements from each individual plant should be collected over a longer period. However, the authors were restricted by logistical constraints related to greenhouse availability and access to the *Gerbera* daisies. Nonetheless, calibrating the thermal camera for the specific *Gerbera* daisies improved the quantitative ST measurements of individual plants when considering a data set of four or eight individual measurements.

There are numerous factors that could contribute to the increased RMSE of the stem. First, the positioning of the thermal camera may have varied between measurements such that the fraction of reflected radiation influencing the microbolometer detector skewed observed STs. Likewise, the positioning of the thermocouple may not be fully representative of the stem ST. The emissivity of the plant organs were not considered during calibration and can affect the ST calculation considering Eq. (3). The camera's emissivity value was fixed at 0.95 for all images captured. Emissivity values for vegetation and plant material are well reported in literature. For instance, Costa et al. [49] noted that plant material has an emissivity value between 0.91 and 0.97, Chen [50] determined that leaf emissivity for three different crops ranged between 0.97 and 0.98, and Harrap et al. [1] noted that an emissivity value of 0.98 is suitable for vegetation and floral tissue [51–54]. Similarily, Huo et al. [55] noted that emissivity of vegetation is generally set to 0.97, however emissivity is variable for plants in nature. The assumed emissivity value of 0.95 falls within the typical range for vegetation and floral tissue. However, an in situ method to quantify emissivity of individual plant organs should be investigated to improve radiometric imaging accuracy.

Concurrent, ongoing research on *Gerbera* daisies, has noted that *Gerbera* daisy stems within the same plant can vary structurally. Similarly, *Gerbera* daisy stems between plants of the same variety are noted to be variable [56]. This phenomenon is different when compared to certain varieties of *Gerbera* daisy flowers. For instance, the Prestige variety has a uniform flower color pattern. Perhaps ST variation and affiliated statistical parameters would be apparent in a *Gerbera* daisy variety with non-uniform flower color patterns. The mechanical differences of the Prestige stems may have impacted the calibrated ST statistics. As a result, for reliable quantitative stem ST measurements, stems of individual *Gerbera* daisies should be calibrated independently from other plants within the same variety.

Other extenuating environmental and equipment factors and limitations may have contributed to inaccuracies within the quantified bias and RMSE values. Firstly, environments with an elevated relative humidity can result in increased inaccuracies of measured surface

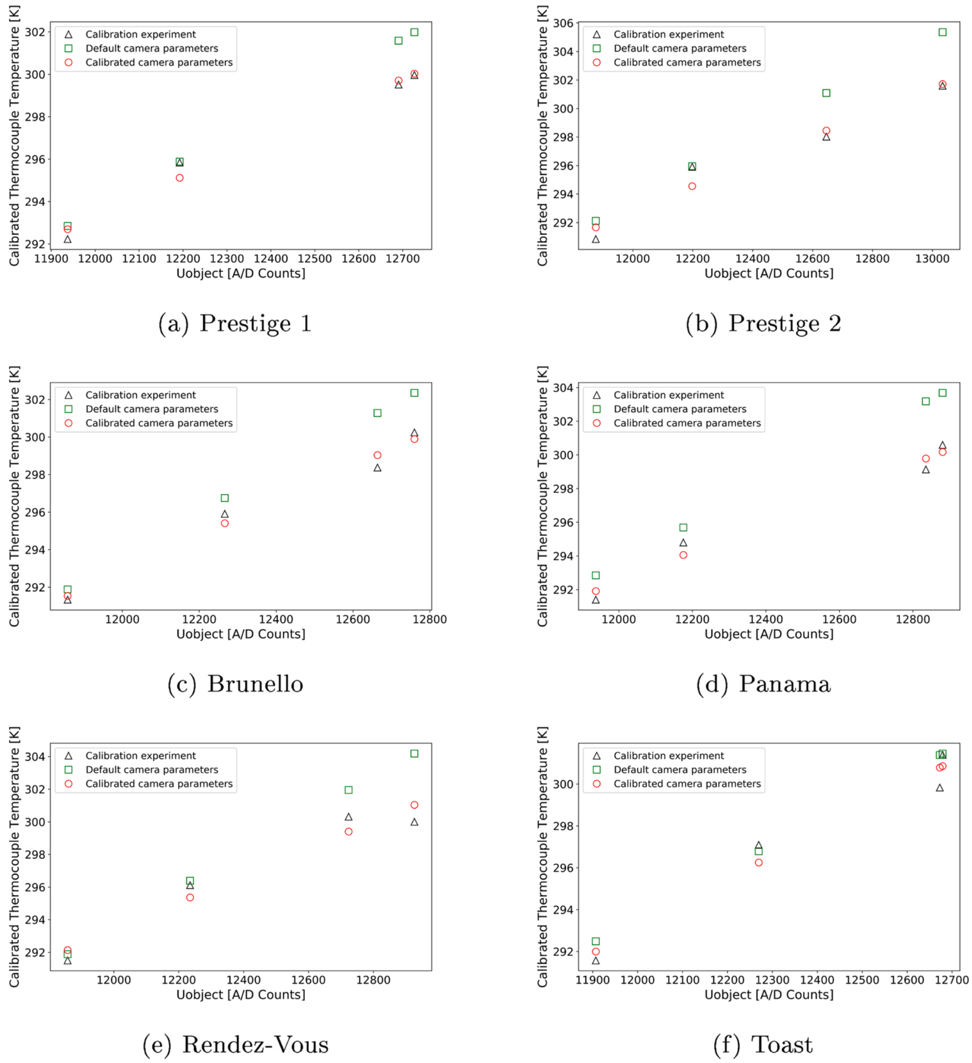

(a) Prestige 1 (b) Prestige 2 (c) Brunello (d) Panama (e) Rendez-Vous (f) Toast

Fig. 6. Thermocouple temperature compared to radiometric image A/D counts values for the calibration experiment (black triangles), the default camera constants (green squares), and the calibrated camera constants (red circles) for each *Gerbera* daisy flower. The calibrated camera constants were used to quantify the calibrated temperatures. (For interpretation of the references to color in this figure legend, the reader is referred to the web version of this article.)

Table 2
Default and calibrated camera parameters.

Gerbera daisy variety/organ	*R*	*B*	*O*	*F*
Default	493,285	1336	− 6707	1.6
Prestige (1) stem	739,927	1319	− 3354	1.6
Prestige (2) stem	739,918	1351	− 4466	1.6
Brunello stem	739,926	1402	− 5760	1.6
Panama stem	739,927	1311	− 3354	1.6
Rendez-Vous stem	739,927	1316	− 3354	1.6
Toast stem	739,927	1461	− 6829	1.6
Prestige combined stem	739,927	1315	− 3354	1.6
Prestige (1) flower	739,926	1400	− 5671	1.6
Prestige (2) flower	739,927	1377	− 5198	1.6
Brunello flower	739,926	1397	− 5640	1.6
Panama flower	739,927	1378	− 5244	1.6
Rendez-Vous flower	739,927	1362	− 4751	1.6
Toast flower	521,244	1350	− 6707	1.6
Prestige combined flower	739,927	1384	− 5328	1.6

Table 3
Default and calibrated camera statistics for stems.

Gerbera daisy variety	Default bias (K)	Default RMSE (K)	Calibrated bias (K)	Calibrated RMSE (K)
Prestige (1)	− 0.64	0.32	0.06	0.03
Prestige (2)	1.01	0.50	0.08	0.04
Brunello	1.46	0.73	− 0.05	0.02
Panama	1.22	0.61	0.03	0.01
Rendez-Vous	0.61	0.31	0.18	0.09
Toast	0.20	0.10	0.09	0.04
Average	0.64	0.43	0.07	0.04

temperature from uncooled thermal cameras [36]. For *Gerbera* daisies, evapotranspiration of the imaged and adjacent plants could have contributed to the elevated measured surface temperatures. For instance, *Gerbera* daisies are noted to have stomata on floral organs [57]. Additionally, relative humidity gradients extending from opening flowers to the floral surroundings are noted to occur in certain flower species [58–60,2,61]. In the greenhouse, over the entire imaging period, *Gerbera* daisies proximal to the imaged flowers were flowering. The air circulation in the greenhouse, especially adjacent to the canopy, may have introduced air with an increased relative humidity (relative to the

Table 4
Default and calibrated camera statistics for flowers.

Gerbera daisy variety	Default bias (K)	Default RMSE (K)	Calibrated bias (K)	Calibrated RMSE (K)
Prestige (1)	1.19	0.59	− 0.11	0.05
Prestige (2)	2.03	1.02	− 0.05	0.02
Brunello	1.60	0.80	− 0.04	0.02
Panama	2.37	1.18	0.05	0.02
Rendez-Vous	1.62	0.81	0.09	0.05
Toast	0.56	0.28	-4×10^{-3}	2×10^{-3}
Average	1.56	0.78	− 0.01	0.03

ambient relative humidity) to the field of view of the thermal camera, thus potentially resulting in an overestimation of object temperature. The degree to which relative humidity and other atmospheric effects impacted the thermal camera in the greenhouse are difficult to quantify. Considering Eq. (3), U_{Atm} accounts for relative humidity effects. This term however must not affect the total thermal camera measurement as it is a function of transmissivity which can generally be estimated as 1, such that the term is omitted from the relation [46]. However, the impact of environmental effects on the surface temperatures derived from thermal images were accounted for due to the in situ nature of the thermal camera calibration.

Beyond atmospheric effects, the FLIR E6 camera used in this study had equipment limitations which impacted the measured object temperature and the calculated bias and RMSE statistics. The thermal resolution of the FLIR E6 camera is 160 by 120 which is quite low as uncooled thermal camera resolutions typically range from 160 by 120 to 1280 by 1024 [62]. Furthermore, Focal-Plane Array thermal cameras are also known to receive errant radiation primarily due to the size-of-source effect [63]. When analyzing the thermal images, a 4 by 4 pixel box was positioned around the thermocouple. This resolution was selected to include sufficient pixels for surface temperature measurement. FLIR Systems recommends using at least a 3 by 3 pixel box [64]. With a 4 by 4 pixel box and an approximate object distance from the camera of 30 cm, the spot size ratio was calculated to be 0.624 cm, based on FLIR Systems [64], which is larger than the diameter of the thermocouple of 0.051 cm. The calibration completed does not consider these errors due to equipment limitations, however, the outcomes of this study still have merit. In the literature, other studies have used low resolution thermal cameras for quantitative work [13,30,65]. Another study completed with a higher resolution uncooled thermal imaging camera (640 by 512) noted the over-estimation of measured surface temperatures [23]. In order to reduce these errors introduced by equipment limitations, a second experiment with a higher resolution thermal camera should be completed following the same methodology, perhaps with more images over a longer time period. A higher resolution thermal camera will increase measurement accuracy and develop a more reliable in situ calibration procedure.

4. Conclusion and future work

An in situ calibration of an uncooled thermal camera was completed to improve Surface Temperature (ST) measurement accuracy of *Gerbera jamesonii* (*Gerbera* daisy) stems and flowers at a commercial greenhouse in Grimsby, Ontario, Canada. A calibrated thermocouple was used, and a thermal image of the thermocouple was recorded over four different days during January–March 2020. New calibration constants intrinsic to the thermal camera were derived for both flowers and stems for each *Gerbera* daisy variety. Bias and root mean square error (RMSE) of the STs considering default manufacturer camera constants and the calibrated camera constants were calculated and compared. For individual plant organs, the averaged calibrated camera constant bias and RMSE values were reduced by at least 89.1% relative to the averaged default camera constant bias and RMSE values. Calibration constants were also derived for the stem and flower of separate *Gerbera* daisy plants of the same

Table 5
Default and calibrated camera statistics considering the STs from the two Prestige plants.

Plant Organ	Default bias (K)	Default RMSE (K)	Calibrated bias (K)	Calibrated RMSE (K)
Stem	0.18	0.06	− 0.06	0.02
Flower	1.61	0.57	− 0.05	0.02

Table 6
Default and calibrated camera statistics considering Prestige constants for one Prestige plant and temperature data for the other Prestige plant.

Prestige plant case/ plant organ	Default bias (K)	Default RMSE (K)	Calibrated bias (K)	Calibrated RMSE (K)
Prestige (1) data/ Prestige (2) constants stem	− 0.64	0.32	− 1.50	0.75
Prestige (1) data/ Prestige (2) constants flower	1.19	0.59	− 0.77	0.38
Prestige (2) data/ Prestige (1) constants stem	1.01	0.50	1.62	0.81
Prestige (2) data/ Prestige (1) constants flower	2.03	1.02	0.64	0.32
Stem average	0.19	0.41	0.06	0.78
Flower average	1.61	0.81	− 0.07	0.35

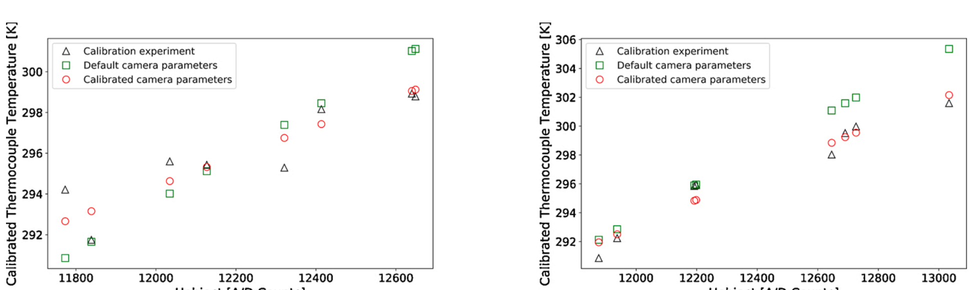

(a) Stem (b) Flower

Fig. 7. Thermocouple temperature compared to radiometric image A/D counts values for the calibration experiment (black triangles), the default camera constants (green squares), and the calibrated camera constants (red circles) for the combined Prestige stems (a) and flowers (b). The calibrated camera constants were used to quantify the calibrated temperatures. (For interpretation of the references to color in this figure legend, the reader is referred to the web version of this article.)

variety where constants were used from one plant and ST data was used from the other plant. Considering this scenario, the averaged calibrated biases for the stem and the flower decreased relative to the averaged default bias and RMSE values by 68.4% and 104.3% respectively. The RMSE statistics for the flower decreased in value, by 56.8%, while the calibrated statistics for the stem increased in value, by 90.2%, relative to the default constants. This discrepancy may be attributed to the sensitivity of the RMSE calculation to outliers due to the limited sample size of the data set. Structural variation of the *Gerbera* daisy stems within the same variety may have also contributed to the increased RMSE value. Environmental effects such as relative humidity and equipment limitations may have influenced the results of this study. A second study is being planned where a higher resolution thermal camera will be used following the method described in this paper to calibrate the camera with respect to surface temperatures of different plant organs over a longer time period.

This paper helps demonstrate the importance of considering environmental impacts on uncooled thermal cameras in relation to accurate quantitative radiometric imaging applications. Likewise, this method has the potential to be applied to calibrate other uncooled thermal cameras for additional quantitative radiometric imaging applications such as the characterization of agricultural crops with respect to sugar or acid content, fever detection within humans, and cancer screening within animals and humans.

Authors' contribution

Ryan A.E. Byerlay: conceptualization, methodology, formal analysis, investigation, data curation, writing – original & draft, writing – review & editing, visualization. Charlotte Coates: methodology, investigation, writing – original & draft, writing – review & editing. Amir A. Aliabadi: writing – review & editing. Peter G. Kevan: resources, writing – review & editing, supervision, funding acquisition.

Funding

This project is part of the Accelerating Green Plant Innovation for Environmental and Economic Benefit Cluster and is funded by the Canadian Ornamental Horticulture Alliance (COHA-ACHO) and by the Government of Canada under the Canadian Agricultural Partnership's AgriScience Program. An NSERC-Discovery Grant (Natural Sciences and Engineering Research Council of Canada) was also used to finance activities of the reported research.

Conflict of interest

No potential conflict of interest was reported by the authors.

Declaration of Competing Interest

The authors report no declarations of interest.

Acknowledgements

The authors thank the staff at Van Geest Bros. Limited for enabling this research to be conducted on their greenhouse premises. Special credit is directed towards Bryan van Geest and John van Eck for the siting of research equipment and selection of plant varieties at the greenhouse facility. Data collection assistance provided by Sean Ratcliffe and technical discussions with Amir Nazem are appreciated.

References

[1] M.J. Harrap, S.A. Rands, N. Hempel de Ibarra, H.M. Whitney, The diversity of floral temperature patterns, and their use by pollinators, eLife 6 (2017) e31262, https://doi.org/10.7554/eLife.31262.
[2] C.J. van der Kooi, P.G. Kevan, M.H. Koski, The thermal ecology of flowers, AoB Plants 124 (2019) 343–353, https://doi.org/10.1093/aob/mcz073.
[3] D. Scherrer, C. Körner, Topographically controlled thermal-habitat differentiation buffers alpine plant diversity against climate warming, J. Biogeogr. 38 (2011) 406–416, https://doi.org/10.1111/j.1365-2699.2010.02407.x.
[4] M. Boukhabla, D. Alkama, Impact of vegetation on thermal conditions outside, thermal modeling of urban microclimate, case study: the street of the Republic, Biskra, Energy Proc. 18 (2012) 73–84, https://doi.org/10.1016/j.egypro.2012.05.019.
[5] P. D'Odorico, Y. He, S. Collins, S.F.J.D. Wekker, V. Engel, J.D. Fuentes, Vegetationmicroclimate feedbacks in woodland-grassland ecotones, Global Ecol. Biogeogr. 22 (2013) 364–379, https://doi.org/10.1111/geb.12000.
[6] S. Khanal, J. Fulton, S. Shearer, An overview of current and potential applications of thermal remote sensing in precision agriculture, Comput. Electron. Agric. 139 (2017) 22–32, https://doi.org/10.1016/j.compag.2017.05.001.
[7] G. Duveiller, J. Hooker, A. Cescatti, The mark of vegetation change on earth's surface energy balance, Nat. Commun. 9 (2018) 679, https://doi.org/10.1038/s41467-017-02810-8.
[8] M. Moradi, B. Dyer, A. Nazem, M.K. Nambiar, M.R. Nahian, B. Bueno, C. Mackey, S. Vasanthakumar, N. Nazarian, E.S. Krayenhoff, L.K. Norford, A.A. Aliabadi, The vertical city weather generator (VCWG v1.0.0), Geosci. Model Dev. Discuss. (2019), https://doi.org/10.5194/gmd-2019-176 (in review).
[9] W.P. Kustas, J.M. Norman, M.C. Anderson, A.N. French, Estimating subpixel surface temperatures and energy fluxes from the vegetation index-radiometric temperature relationship, Remote Sens. Environ. 85 (2003) 429–440, https://doi.org/10.1016/S0034-4257(03)00036-1.
[10] Q. Liu, C. Yan, Q. Xiao, G. Yan, L. Fang, Separating vegetation and soil temperature using airborne multiangular remote sensing image data, Int. J. Appl. Earth Obs. 17 (2012) 66–75, https://doi.org/10.1016/j.jag.2011.10.003.
[11] F. Meier, D. Scherer, J. Richters, A. Christen, Atmospheric correction of thermal-infrared imagery of the 3-D urban environment acquired in oblique viewing geometry, Atmos. Meas. Tech. 4 (2011) 909–922, https://doi.org/10.5194/amt-4-909-2011.
[12] K. Kusnierek, A. Korsaeth, Challenges in using an analog uncooled microbolometer thermal camera to measure crop temperature, Int. J. Agric. Biol. Eng. 7 (2014) 60–74, https://doi.org/10.3965/j.ijabe.20140704.007.
[13] I. Lamprecht, C. Maierhofer, M. Röllig, A thermographic promenade through the Berlin Botanic Garden, Thermochim. Acta 446 (2006) 4–10, https://doi.org/10.1016/j.tca.2006.02.039.
[14] F. van der Meer, Near-infrared laboratory spectroscopy of mineral chemistry: a review, Int. J. Appl. Earth Obs. 65 (2018) 71–78, https://doi.org/10.1016/j.jag.2017.10.004.
[15] V. Dhar, Z. Khan, Comparison of modeled atmosphere-dependent range performance of long-wave and mid-wave IR imagers, Infrared Phys. Techn. 51 (2008) 520–527, https://doi.org/10.1016/j.infrared.2008.05.001.
[16] J.A. Schultz, M. Hartmann, S. Heinemann, J. Janke, C. Jürgens, D. Oertel, G. Rücker, F. Thonfeld, A. Rienow, DIEGO: a multispectral thermal mission for earth observation on the International Space Station, Eur. J. Remote Sens. (2019) 1–11, https://doi.org/10.1080/22797254.2019.1698318.
[17] J. Peckham, S. O'Young, J.T. Jacobs, Comparison of medium and long wave infrared imaging for ocean based sensing, J. Ocean Technol. 10 (2015) 113–128.
[18] K. Ribeiro-Gomes, D. Hernández-López, J.F. Ortega, R. Ballesteros, T. Poblete, M. A. Moreno, Uncooled thermal camera calibration and optimization of the photogrammetry process for UAV applications in agriculture, Sesnors-Basel 17 (2017) 2173, https://doi.org/10.3390/s17102173.
[19] H. Sheng, H. Chao, C. Coopmans, J. Han, M. McKee, Y. Chen, Low-cost UAV-based thermal infrared remote sensing: platform, calibration and applications, Proceedings of 2010 IEEE/ASME International Conference on Mechatronic and Embedded Systems and Applications (2010) 38–43.
[20] H. Budzier, G. Gerlach, Calibration of uncooled thermal infrared cameras, J. Sens. Syst. 4 (2015) 187–197, https://doi.org/10.5194/jsss-4-187-2015.
[21] FLIR-Systems, The Ultimate Infrared Handbook for R&D Professionals, 2012 (Last accessed 18 March 2020).
[22] D. Lin, H.-G. Mass, P. Westfeld, H. Budzier, G. Gerlach, An advanced radiometric calibration approach for uncooled thermal cameras, Photogramm. Rec. 33 (2018) 30–48, https://doi.org/10.1111/phor.12216.
[23] R.A.E. Byerlay, M.K. Nambiar, A. Nazem, M.R. Nahian, M. Biglarbegian, A. A. Aliabadi, Measurement of land surface temperature from oblique angle airborne thermal camera observations, Int. J. Remote Sens. 41 (2020) 3119–3146, https://doi.org/10.1080/01431161.2019.1699672.
[24] S. Gallardo-Saavedra, L. Hernández-Callejo, O. Duque-Perez, Technological review of the instrumentation used in aerial thermographic inspection of photovoltaic plants, Renew. Sustain. Energy Rev. 93 (2018) 566–579, https://doi.org/10.1016/j.rser.2018.05.027.
[25] J. Kelly, N. Kljun, P.-O. Olsson, L. Mihai, B. Liljeblad, P. Weslien, L. Klemedtsson, L. Eklundh, Challenges and best practices for deriving temperature data from an uncalibrated UAV thermal infrared camera, Remote Sens.-Basel 11 (2019) 567, https://doi.org/10.3390/rs11050567.
[26] P.G. Kevan, P. Nunes-Silva, R. Sudarsan, Short communication: thermal regimes in hollow stems of herbaceous plants-concepts and models, Int. J. Biometeorol. 62 (2018) 2057–2062, https://doi.org/10.1007/s00484-018-1602-7.
[27] A. Coupel-Ledru, B. Pallas, M. Delalande, F. Boudon, E. Carrié, S. Martinez, J.-L. Regnard, E. Costes, Multi-scale high-throughput phenotyping of apple architectural and functional traits in orchard reveals genotypic variability under contrasted watering regimes, Hortic. Res. 6 (2019), https://doi.org/10.1038/s41438-019-0137-3.

[28] A. Martynenko, K. Shotton, T. Astatkie, G. Petrash, C. Fowler, W. Neily, A. T. Critchley, Thermal imaging of soybean response to drought stress: the effect of *Ascophyllum nodosum* seaweed extract, SpringerPlus 5 (2016) 1393, https://doi.org/10.1186/s40064-016-3019-2.
[29] S. Zia, G. Romano, W. Spreer, C. Sanchez, J. Cairns, J.L. Araus, J. Müller, Infrared thermal imaging as a rapid tool for identifying water-stress tolerant maize genotypes of different phenology, J. Agro. Crop Sci. 199 (2013) 75–84, https://doi.org/10.1111/j.1439-037X.2012.00537.x.
[30] M.H. Kapanigowda, R. Perumal, M. Djanaguiraman, R.M. Aiken, T. Tesso, P.V. V. Prasad, C.R. Little, Genotypic variation in sorghum [*Sorghum bicolor* (L.) Moench] exotic germplasm collections for drought and disease tolerance, SpringerPlus 2 (2013) 650, https://doi.org/10.1186/2193-1801-2-650.
[31] J. Bellvert, P.J. Zarco-Tejada, J. Girona, E. Fereres, Mapping crop water stress index in a 'Pinot-noir' vineyard: comparing ground measurements with thermal remote sensing imagery from an unmanned aerial vehicle, Precis. Agric. 15 (2014) 361–376, https://doi.org/10.1007/s11119-013-9334-5.
[32] S. Fuentes, R.D. Bei, J. Pech, S. Tyerman, Computational water stress indices obtained from thermal image analysis of grapevine canopies, Irrig. Sci. 30 (2012) 523–536, https://doi.org/10.1007/s00271-012-0375-8.
[33] F.-J. Mesas-Carrascosa, F. Pérez-Porras, J.E.M. de Larriva, C.M. Frau, F. Agüera-Vega, F. Carvajal-Ramírez, P. Martínez-Carricondo, A. García-Ferrer, Drift correction of lightweight microbolometer thermal sensors on-board unmanned aerial vehicles, Remote Sens.-Basel 10 (2018) 615, https://doi.org/10.3390/rs10040615.
[34] FLIR-Systems, Seeing Through Fog and Rain With A Thermal Imaging Camera, Metrological Effects of Fog & Rain Upon IR Camera Performance, Technical Note (Last accessed 19 May 2020).
[35] K. Wang, R.E. Dickinson, Global atmospheric downward longwave radiation at the surface from ground-based observations, satellite retrievals, and reanalyses, Rev. Geophys. 51 (2013) 150–185, https://doi.org/10.1002/rog.20009.
[36] D.L. Mangus, A. Sharda, Selection and utility of uncooled thermal cameras for spatial crop temperature measurement within precision agriculture, Proceedings of the 13th International Conference on Precision Agriculture (2016) 1–16.
[37] C.E. Torgersen, R.N. Faux, B.A. McIntosh, N.J. Poage, D.J. Norton, Airborne thermal remote sensing for water temperature assessment in rivers and streams, Remote Sens. Environ. 76 (2001) 386–398, https://doi.org/10.1016/S0034-4257(01)00186-9.
[38] S.J. Dugdale, A practitioner's guide to thermal infrared remote sensing of rivers and streams: recent advances, precautions and considerations, WIREs Water 3 (2016) 251–268, https://doi.org/10.1002/wat2.1135.
[39] E.A. Baker, L.K. Lautz, J.M. McKenzie, C. Aubry-Wake, Improving the accuracy of time-lapse thermal infrared imaging for hydrologic applications, J. Hydrol. 571 (2019) 60–70, https://doi.org/10.1016/j.jhydrol.2019.01.053.
[40] J.A. Sobrino, J. Cuenca, Angular variation of thermal infrared emissivity for some natural surfaces from experimental measurements, Appl. Opt. 38 (1999) 3931–3936, https://doi.org/10.1364/AO.38.003931.
[41] J.A. Sobrino, J.C. Jiménez-Muñoz, W. Verhoef, Canopy directional emissivity: comparison between models, Remote Sens. Environ. 99 (2005) 304–314, https://doi.org/10.1016/j.rse.2005.09.005.
[42] M.R. James, S. Robson, H. Pinkerton, M. Ball, Oblique photogrammetry with visible and thermal images of active lava flows, Bull. Volcanol. 69 (2006) 105–108, https://doi.org/10.1007/s00445-006-0062-9.
[43] M. Ball, H. Pinkerton, Factors affecting the accuracy of thermal imaging cameras in volcanology, J. Geophys. Res. Solid Earth 111 (2006) B11203, https://doi.org/10.1029/2005JB003829.
[44] FLIR-sUAS, Radiometric Temperature Measurements, FLIR Systems, 2016 (Last accessed 16 April 2020).
[45] R. Olbrycht, B. Więcek, New approach to thermal drift correction in microbolometer thermal cameras, Quant. Infr. Therm. J. 12 (2) (2015) 184–195.
[46] R. Usamentiaga, P. Venegas, J. Guerediaga, L. Vega, J. Molleda, F.G. Bulnes, Infrared thermography for temperature measurement and non-destructive testing, Sensors-Basel 14 (7) (2014) 12305–12348.
[47] G.M. Smith, E.J. Milton, The use of the empirical line method to calibrate remotely sensed data to reflectance, Int. J. Remote Sens. 20 (13) (1999) 2653–2662.
[48] T. Chai, R.R. Draxler, Root mean square error (RMSE) or mean absolute error (MAE)? Arguments against avoiding RMSE in the literature, Geosci. Model Dev. 7 (2014) 1247–1250, https://doi.org/10.5194/gmd-7-1247-2014.
[49] J.M. Costa, O.M. Grant, M.M. Chaves, Thermography to explore plant-environmental interactions, J. Exp. Bot. 64 (13) (2013) 3937–3949, https://doi.org/10.1093/jxb/ert029.
[50] C. Chen, Determining the leaf emissivity of three crops by infrared thermometry, Sensors-Basel 15 (2015) 11387–11401, https://doi.org/10.3390/s150511387.
[51] E. Rubio, V. Caselles, C. Badenas, Emissivity measurements of several soils and vegetation types in the 8-14 μm wave band: analysis of two field methods, Remote Sens. Environ. 59 (3) (1997) 490–521, https://doi.org/10.1016/S0034-4257(96)00123-X.
[52] A. Rejšová, J. Brom, J. Pokorný, J. Korečko, Temperature distribution in light-coloured flowers and inflorescences of early spring temperate species measured by infrared camera, Flora 205 (4) (2010) 282–289, https://doi.org/10.1016/j.flora.2009.05.001.
[53] A. López, F.D. Molina-Aiz, D.L. Valera, A. Peña, Determining the emissivity of the leaves of nine horticultural crops by means of infrared thermography, Sci. Hortic. 1 (2012) 49–58, https://doi.org/10.1016/j.scienta.2012.01.022.
[54] L. Dietrich, C. Körner, Thermal imaging reveals massive heat accumulation in flowers across a broad spectrum of alpine taxa, Alp. Bot. 124 (2014) 27–35, https://doi.org/10.1007/s00035-014-0123-1.
[55] H. Huo, Z.-L. Li, Z. Xing, Temperature/emissivity separation using hyperspectral thermal infrared imagery and its potential for detecting the water content of plants, Int. J. Remote Sens. 40 (2019) 1672–1692, https://doi.org/10.1080/01431161.2018.1513668.
[56] U. van Meeteren, Water relations and keeping-quality of cut gerbera flowers. I. The cause of stem break, Sci. Hortic. 8 (1978) 65–74, https://doi.org/10.1016/0304-4238(78)90071-7.
[57] X. Huang, S. Lin, S. He, X. Lin, J. Liu, R. Chen, Characterization of stomata on floral organs and scapes of cut 'real' gerberas and their involvement in postharvest water loss, Postharvest Biol. Technol. 142 (2018) 39–45, https://doi.org/10.1016/j.postharvbio.2018.04.001.
[58] S.A. Corbet, Bee visits and the nectar of *Echium vulgare* L. and *Sinapis alba* L, Ecol. Entomol. 3 (1978) 25–37, https://doi.org/10.1111/j.1365-2311.1978.tb00900.x.
[59] S.A. Corbet, D.M. Unwin, O.E. Prŷs-Jones, Humidity, nectar and insect visits to flowers, with special reference to *Crataegus*, *Tilia* and *Echium*, Ecol. Entomol. 4 (1979) 9–22, https://doi.org/10.1111/j.1365-2311.1979.tb00557.x.
[60] M. von Arx, J. Goyret, G. Davidowitz, R.A. Raguso, Floral humidity as a reliable sensory cue for profitability assessment by nectar-foraging hawkmoths, Proc. Natl. Acad. Sci. U.S.A. 109 (2012) 9471–9476, https://doi.org/10.1073/pnas.1121624109.
[61] M.J.M. Harrap, N.H. de Ibarra, H.D. Knowles, H.M. Whitney, S.A. Rands, Floral humidity in flowering plants: a preliminary survey, Front. Plant Sci. 11 (2020) 249, https://doi.org/10.3389/fpls.2020.00249.
[62] R. Gade, T.B. Moeslund, Thermal cameras and applications: a survey, Mach. Vision Appl. 25 (2014) 245–262, https://doi.org/10.1007/s00138-013-0570-5.
[63] M.J. Hobbs, C. Zhu, M.P. Grainger, C.H. Tan, J.R. Willmott, Quantitative traceable temperature measurement using novel thermal imaging camera, Opt. Express 26 (19) (2018) 24904–24916, https://doi.org/10.1364/OE.26.024904.
[64] FLIR-Systems, Technical Note: How Far Can You Measure? Considering Spot Size Ratio is Key, 2018 (Last accessed 20 August 2020).
[65] R.A. Senior, J.K. Hill, D.P. Edwards, ThermStats: an R package for quantifying surface thermal heterogeneity in assessments of microclimates, Methods Ecol. Evol. 10 (9) (2019) 1606–1614, https://doi.org/10.1111/2041-210X.13257.